

Atomic Lattice Resolved Electron Tomography of a 3D Self-Assembled Mesocrystal

Xiaolei Chu, Alex Abelson, Caroline Qian, Oleg Igouchkine, Ethan Field, Kwan-Liu Ma, Matt Law, and Adam J. Moule*

Complex 3D architectures of nanoscale building blocks can be created by self-assembly, but characterization of the atomic to mesoscale structure of such materials is limited by the difficulty of visualizing atoms across multiple length scales. Here, scanning transmission electron microscopy (STEM) and full-tilt tomographic reconstruction are used to image a single-crystalline region of a 3D epitaxially-fused PbSe quantum dot (QD) superlattice containing 633 QDs at a spatial resolution of 2.16 Å. The combined real-space and reciprocal-space analysis enables 3D mesoscale correlations of atomic lattice and superlattice order across hundreds of nanocrystals in 3D for the first time. Inhomogeneity in QD positional and orientational order reveals that the QD surface layers template the superlattice and that orientational entropy is higher in the interior layers than the surface layers. The measurement and analysis techniques presented here are applicable to a broad range of 3D nanostructured materials.

(zeolites^[1,2] and metal–organic frameworks^[3]), hydrogen production^[4] and storage,^[2] emerging photovoltaics,^[5–7] electricity storage (batteries^[8] and supercapacitors^[9]), and structural metals.^[10,11] However, nanostructured materials are difficult to characterize because their macroscopic properties arise from hierarchical structures that span considerable length scales (0.01–1000 nm). Recent advances in atom probe tomography,^[12–14] X-ray ptychography,^[15,16] and electron tomography (ET)^[17–20] have increasingly enabled structural and chemical mapping of nanomaterials over mesoscopic length scales. All-atom counting techniques have been used to identify every atom in single-crystalline and polycrystalline

1. Introduction

Nanostructured materials with ordering across multiple length scales are increasingly studied for application in catalysis

nanocrystals^[21,22] as well as nanocrystal monolayers.^[23] 4D scanning transmission electron microscopy (STEM) combines real-space and convergent beam electron diffraction imaging, but does not enable resolution of depth information.^[23–26] Here, we present the first demonstration of nanocrystal-by-nanocrystal orientation analysis from lattice-resolved ET, which combines real-space imaging and reciprocal-space analysis resolved in all three spatial dimensions, using a self-assembled 3D epitaxially-fused superlattice (epi-SL) of PbSe QDs as a test sample. Using a tomogram with a spatial resolution of 2.16 Å, we determine the orientation and local lattice parameters of the superlattice (SL), the orientation of the atomic lattice (AL) of each QD, and the number, size, and shape of the epitaxial connections (necks) between the QDs. The clear breakthrough is the new ability to map position/orientation anisotropy from atomic-to meso-scale, which is critical knowledge for characterization of 3D-nanostructured materials.

To demonstrate atomic lattice resolved electron tomography on the mesoscale, we acquired and analyzed a full-tilt ET dataset for a multilayer (3D) PbSe QDs epi-SL. Epi-SLs are crystals of colloidal QDs with exceptionally high spatial order. The high spatial order and ordered epitaxial necks between nearest neighbor QDs provide for strong inter-QD electronic coupling, making epi-SLs promising materials for exhibiting delocalized electronic mini-bands and serving as a versatile class of QD solids for next-generation optoelectronics.^[27–32] However, current epi-SLs contain significant concentrations of structural defects (variations in QD position and orientation, the number, size and shape of necks, and QD size and shape) that localize carriers and prevent coherent electronic transport. Rational

X. Chu, E. Field
Department of Materials Science and Engineering
University of California - Davis
Davis, CA 95616, USA

A. Abelson, M. Law
Department of Materials Science and Engineering
University of California - Irvine
Irvine, CA 92697, USA

C. Qian, M. Law
Department of Chemical and Biomolecular Engineering
University of California - Irvine
Irvine, CA 92697, USA

O. Igouchkine, K.-L. Ma
Department of Applied Math
University of California - Davis
Davis, CA 95616, USA

M. Law
Department of Chemistry
University of California - Irvine
Irvine, CA 92697, USA

A. J. Moule
Department of Chemical Engineering
University of California - Davis
Davis, CA 95616, USA
E-mail: amoule@ucdavis.edu

 The ORCID identification number(s) for the author(s) of this article can be found under <https://doi.org/10.1002/adfm.202301026>.

DOI: 10.1002/adfm.202301026

improvements to synthesis/fabrication of more perfect 3D epi-SLs is contingent upon acquisition of structural information from characterization methods that are capable of mapping defects throughout the volume of an epi-SL and down to the atomic scale, a challenging task. Conventional (S)TEM imaging and diffraction methods cannot provide internal structural details of 3D samples.^[27,28,33,34] ET, in which a 3D object is reconstructed from a series of 2D images taken at a series of tilt angles, has been used to establish the basic unit cell of non-fused unary, binary, and ternary QD SLs^[35–37] as well as 2D honeycomb epi-SLs^[38] and thin multilayer honeycomb epi-SLs,^[39] but none of these tomograms approached atomic resolution. We recently reported an electron tomogram of a polycrystalline 3D epi-SL with a resolution of 6.5 Å, sufficient to see the location, size and shape of all 1846 PbSe QDs and their necks, but not the atomic lattice.^[40] By leveraging improvements in 2D STEM resolution, use of a full-tilt sample holder, reduced FIB needle sample volume, improved reconstruction alignment, and a graphics processing unit (GPU) based computer that was optimized for image reconstruction, we show that it is now possible to produce tomograms of sufficient resolution (2.16 Å) to image the atomic lattice of every QD in a 3D epi-SL and to provide a detailed and accurate map of both the atomic lattice and the superlattice. The unprecedented structural detail of atomic lattice resolved mesoscale ET will enable new insights into processing-structure-property relationships for QD epi-SLs and other nanostructured and mesoscale materials.

2. Results and Discussion

2.1. Mapping QD Positions and Orientations

Several ET 3D reconstructions were created from a series of 2D high-angle annular dark field (HAADF) STEM images taken at different tilt angles. The multilayer (3D) QD epi-SL, fabricated as previously described,^[40,41] was milled into several needles to enable acquisition of images over a full 180° angular range to help avoid reconstruction artifacts.^[42] Figure 1a,b shows SEM images of the epi-SL film on a silicon substrate and the sample #1 tomography needle extracted from the film by focused ion beam (FIB) milling,^[43] respectively. Figure 1c shows one of the 2D STEM projections. The highest resolution 3D tomographic reconstruction was obtained from a 60 nm wide × 40 nm tall disc-shaped epi-SL sample is presented in Figure 1d. Further sample preparation and tomographic reconstruction details can be found in Section S1 (Supporting Information) and a full tilt-series of 2D images and the completed reconstruction are separate movie files in the Supporting Information. Projections and results from a separate tomographic reconstruction from the same film but with lower resolution are also presented in the Supporting Information. The center-of-mass (CoM) positions of all 633 QDs in the sample, described by the vectors $P_i^{\text{SL}} = [x_i, y_i, z_i]$, where i is the QD index, were determined by iteratively convoluting the tomogram with a digital mask of a QD extracted from the original tomogram volume as described in Section S2 (Supporting Information). The SL structure is defined by unit vectors connecting the CoM

positions of nearest-neighbor (NN) QDs as described by the matrix $R_i^{\text{SL}} = [\bar{A}_i, \bar{B}_i, \bar{C}_i]$, where $\bar{A}_i = [100]_{\text{SL}}$, $\bar{B}_i = [010]_{\text{SL}}$ and $\bar{C}_i = [001]_{\text{SL}}$.

The inset of Figure 1d shows an intensity pattern depicting the positions of the Pb atoms. While the lattice fringes of PbSe are clearly visible throughout the volume of the tomogram, it was not possible to resolve every Pb atom in the sample or consistently detect the lighter Se atoms in the background of heavier Pb atoms within this large volume. Instead, we performed a windowed Fourier analysis of the volume around each QD CoM to determine the AL spacing and orientation of each QD in the sample as described in Section S3 (Supporting Information). The inset of Figure 1e shows the 3D FFT of the entire volume with the $\{200\}_{\text{AL}}$ Bragg spots annotated. Figure 1e (blue) shows the 1D power spectrum along with the simulated reference for rock salt PbSe (red). The experimental spectrum shows peaks at spatial frequencies corresponding to PbSe $d_{111} = 3.52$ Å, $d_{200} = 3.05$ Å, and $d_{220} = 2.16$ Å. The spatial resolution of the tomogram is determined to be 1.85–2.16 Å using the visible d_{200} and missing d_{311} diffraction peaks. We converted the Bragg spots in reciprocal space into a set of three mutually-orthonormal AL basis vectors ($R_i^{\text{AL}} = [\bar{a}, \bar{b}, \bar{c}]_i$) that describe the 3D orientation of each QD with an angular uncertainty of 1.9°. Together, P_i^{SL} , R_i^{AL} , and R_i^{SL} provide measurements of the position, AL orientation, and relative SL orientation for each QD, respectively.

2.2. Multi-Dimensional Data Visualization

We used a glyph-stick representation to better represent the position, orientation, and their variance across the epi-SL (Figure 2a–c). In this representation, each cuboid glyph represents a QD centered at P_i^{SL} and oriented at R_i^{AL} , with the cuboid faces representing the $(100)_{\text{AL}}$ planes. The glyph color represents the average orientational misalignment (defined below and in Sections S5 and S7, Supporting Information). We measured the thickness of each epitaxial neck between the QDs and represent the presence of a neck with a stick along the local SL vector connecting QD CoMs. The relative thickness of the neck is represented using the stick color. Figure 2b,c show overlays of tomogram slices and glyph-stick representations for SL layers C1 and C5 (C denotes the plane normal SL lattice direction, C1 is the bottom plane, and C9 is the top plane). This comparison underscores the necessity to represent this highly-complex sample using a visualization that highlights spatial correlations that cannot be directly interpreted by inspection of the tomogram itself. The complete set of raw tomogram slices and corresponding glyph-stick visualizations along all SL lattice directions are provided in Section S4 (Supporting Information).

This epi-SL sample is composed of a single triclinic SL grain with no grain boundaries. The QDs assemble into nine in-plane layers with the $(100)_{\text{SL}}$ plane oriented parallel to the substrate. This sample is more uniform than previously reported 3D PbSe epi-SL samples, which is demonstrated by fewer SL point vacancies or interstitial QDs (2.2% versus 10%), improved QD connectivity (89.3% compared to 75%), and a narrower distribution of neck diameters (± 0.9 nm compared to ± 1.5 nm).^[40]

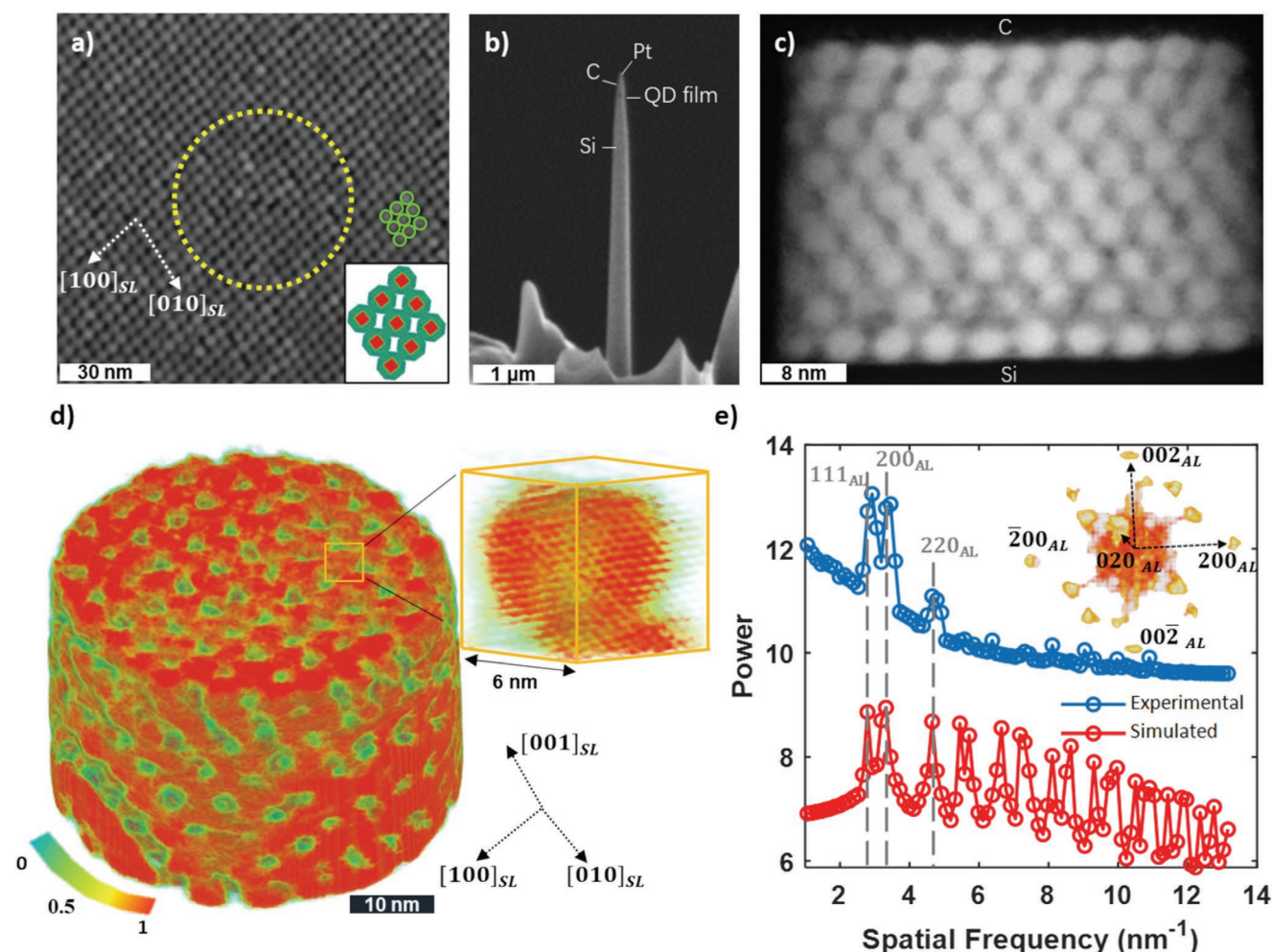


Figure 1. Lattice-resolved electron tomogram of a PbSe QD epi-SL grain: a) SEM image of a $(100)_{\text{SL}}$ -oriented epi-SL grain. The dashed circle denotes the part of the sample that was extracted for electron tomography analysis. The inset images show a model of the surface superlattice structure, with color to highlight the facets of the quantum dots. The white arrows denote the directions of the superlattice vectors $[001]_{\text{SL}}$ and $[010]_{\text{SL}}$. b) SEM image of the FIB-prepared tomography needle. The epi-SL is located near the tip of the silicon needle capped with carbon and platinum from FIB sample preparation. c) A single HAADF-STEM image of the epi-SL disc (≈ 60 nm diameter \times ≈ 40 nm thick). d) Perspective view of the entire tomogram and a magnified view of a single QD demonstrating 3D lattice resolution with the $\{220\}$ lattice fringes clearly visible. The color scale represents normalized intensity value of the tomogram. The dashed arrows provide visual guidance for the three SL directions. e) 1D power spectrum of the 3D Fourier transform of the tomogram (blue) compared to a simulated FFT of the Pb lattice in PbSe (red). The simulated FFT is broadened from the point spread function and represents the upper limit of tomographic resolution considering both thermal and instrumental factors. The vertical dashed lines denote the $\{111\}_{\text{AL}}$, $\{200\}_{\text{AL}}$, and $\{220\}_{\text{AL}}$ planes, corresponding to d-spacings of 3.52, 3.05, and 2.16 Å, respectively. Inset is the 3D power spectrum of the tomogram with all 200 Bragg spots denoted.

A quantitative comparison of all SL unit cell parameters is in Table S2 (Supporting Information).

The lattice-resolved tomogram is a high-resolution map of QD positions, orientations, and necks that can be used to quantify the spatial variability of structural order within the epi-SL. We use components of $R_i^{\text{SL}} = [\bar{A}_i, \bar{B}_i, \bar{C}_i]$ averaged over all QDs in a layer, where C1 is the first layer of the $[001]_{\text{SL}}$. The map shows that the top and bottom QD monolayers of the sample (C1 and C9) are strikingly more perfect than the interior layers (C2–C8). Figure 2a–c illustrates that C1 and C9 are more planar, QDs have less orientational disorder, no point defects, and higher connectivity. Layer planarity was measured by fitting the width of the distribution (FWHM) of the vertical component of each QD position (P^{SL}) versus the layer

index (Figure 2e). We found much smaller FWHM values for C1 and C9 (0.1–0.4 nm) than C2 and C8 (≈ 1.2 nm) and C3–C7 (0.7–1.0 nm). In contrast, the A and B layers had similar planarity throughout the sample (Figure S12, Supporting Information). The large and unique difference in planarity, orientation order, and reduced point defects between the surface layers and interior layers indicates that QDs at the liquid/film and film/gas interfaces experience significant ordering due to ligand/fluid interactions during self-assembly and epi-fusion compared to the QDs in the middle layers of the film. This means specifically that 2D epi-SL samples and surface specific measurement of 3D epi-SLs make poor models for multi-layer QD epi-SLs. Interface layer formation may play a strong role in templating inner layers. Analysis of additional 3D epi-SLs

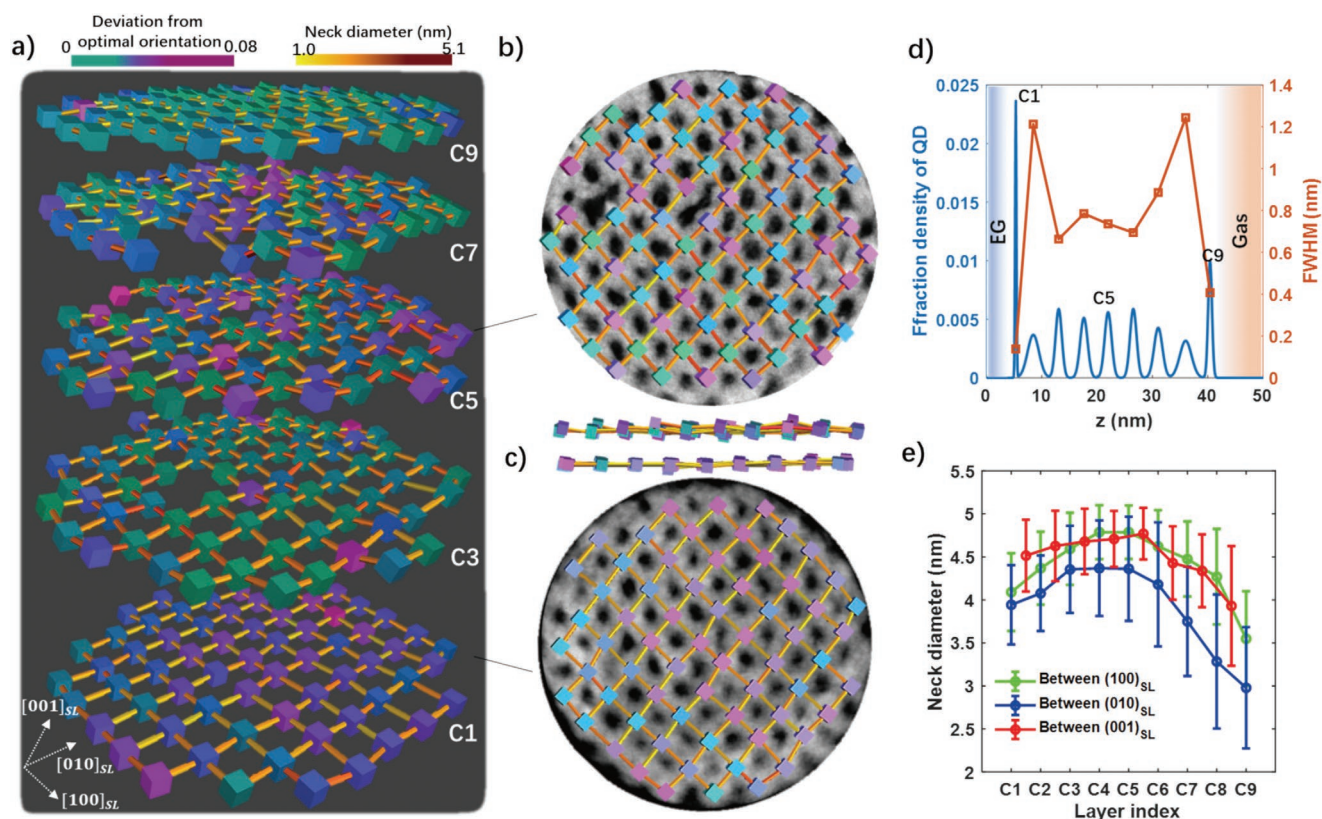


Figure 2. Tomographic visualization of the epi-SL: a) Exploded cube-stick view of every odd $(100)_{SL}$ layer of the sample (C1, C3, C5, C7, and C9). C1 is the bottom layer of the film (formed at the interface with ethylene glycol) and C9 is the top layer of the film (formed at the gas interface). Glyph positions and orientations denote QD positions and orientations, while the sticks represent the necks between QDs. The glyph color indicates QD misorientation relative to R_{AL}^{mono} and the stick color indicates neck diameter. b,c) Plan and side views of C1 and C5. Each plan view shows a tomographic slice overlaid with the glyph-stick model. d) Plot of the distribution of the vertical component of each QD position (blue, left axis) and its FWHM (orange, right axis) for C1–C9. The orange line is a guide to the eye. e) Plot of the average inter-QD neck diameter between $(100)_{SL}$ (green), $(010)_{SL}$ (blue), and $(001)_{SL}$ (red) planes. Error bars represent one standard deviation.

will be needed to determine if this result is general and how to utilize the surface layer templating for fabrication of more ordered epi-SLs over larger domain areas.

Analysis of the neck thicknesses and R_{AL} does not show simple surface/bulk trends. Figure 2e shows the diameters of the necks along all three SL directions. Generally, the neck thickness is, within error, uniform for C1–C6 and then decreases toward the top layer. We expected that a vertical gradient in neck thickness would occur as a result of ligand exchange diffusion from the liquid/liquid interface that would result in thinner necks closer to the top surface of the epi-SL. However, this trend is not clear and may become more relevant for thicker epi-SLs. A careful analysis of Figure 2a reveals systematic and complex changes in R_{AL} as a function of the vertical layer index. C1 and C9 show less variation in AL and SL orientation (i.e., less variance in orientation and color of the cubes within a layer), which is correlated with the higher planarity of these layers. In summary, these observations demonstrate the need for 3D atomistic measurements of QD SLs, that, unlike 2D techniques (SEM, 4D STEM, AFM, STM, etc.), can reveal differences between the structure of surface versus interior layers.

In the following sections, we analyze the AL and SL orientations of the QDs as a function of their position in the epi-SL

for the purpose of understanding how the epi-SL forms during ligand exchange. We know from previous work that the QDs self-assemble into a superlattice in which the atomic lattices of the QDs are aligned because of the attractive/repulsive forces between oleic acid ligands on the QD facets.^[41,44,45] A ligand exchange reaction is used to remove the oleic acid (OA) ligands and leads to a coordinated formation of the triclinic epi-SL measured here. Below, we use mathematical analysis via P^{SL} , R_{AL} , and R_{AL} to understand the formation mechanism of epi-SL structure from the self-assembled SL.

2.3. QD Orientation Analysis (Mesoscale)

In this section, we analyze the orientation distribution of the whole sample using statistical methods in order to derive trends that drive the epi-SL formation across length scales much larger than single QDs. Figure 3a presents stereographic projections of R_{AL} (dark symbols) and R_{SL} (light symbols) for all 633 QDs. Since the AL is cubic, the lattice vectors of the AL are orthogonal. The QDs show excellent orientation uniformity with in-plane and out-of-plane angular spreads of $\approx 3.7^\circ$ and $\approx 11.3^\circ$, respectively. The insets further breakdown the average

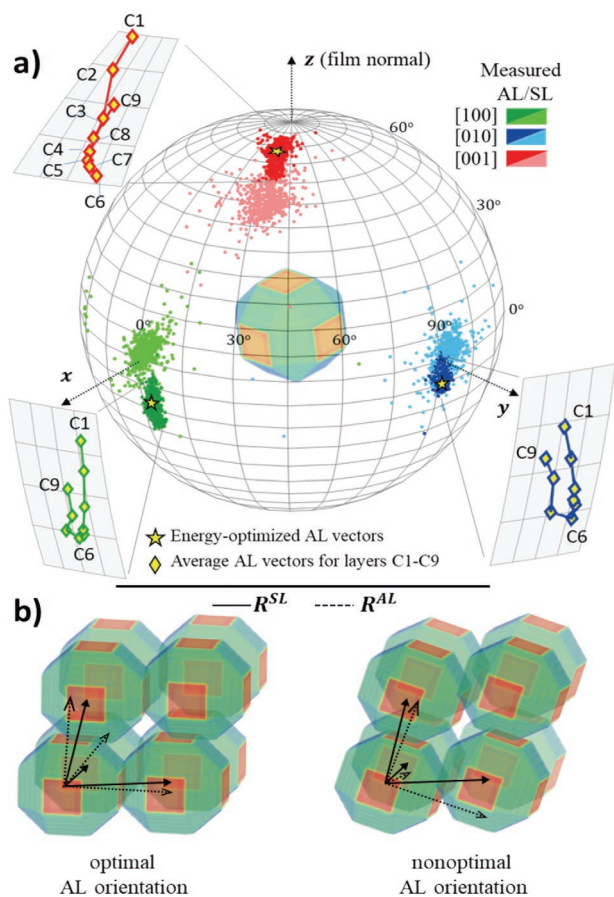


Figure 3. Global map of QD orientations: a) Stereographic projection of the AL and SL lattice vectors of all 633 QDs in the sample relative to the film normal: $[100]_{\text{AL}}$ (green), $[010]_{\text{AL}}$ (blue), $[001]_{\text{AL}}$ (red), $[100]_{\text{SL}}$ (lt green), $[010]_{\text{SL}}$ (lt blue), and $[001]_{\text{SL}}$ (lt red). Stars denote the calculated energy-optimized AL orientation ($R_{\text{mono}}^{\text{AL}}$) for the experimentally-determined SL unit cell. Diamonds are the average AL vectors for each $(001)_{\text{SL}}$ layer (C1–C9). A model of a faceted QD is inset at the center of the projection with its orientation aligned with $R_{\text{mono}}^{\text{AL}}$. b) Comparison of the energy-optimized epi-SL unit cell (more like surface layers) with a non-optimal unit cell (more like internal layers). Solid and dashed lines represent the lattice vectors of the SL and AL, respectively. The SL lattice vectors of the unit cells are identical.

R^{AL} as a function of in-plane layers C1–C9, which in the $[001]_{\text{SL}}$ changes systematically along the film normal (large diamonds in Figure 3a) but not in-plane. This result shows that the R^{AL} tilts systematically out-of-plane from C1 to C6 and back into alignment with the substrate plane from C7 to C9. Each layers' alignment is more uniform than the global average of the full epi-SL. The QDs are most closely aligned to the film normal in layers C1 and C9, suggesting that they are strongly oriented during self-assembly at the liquid/film and film/gas interfaces. The AL orientation changes 8.4° out-of-plane from C2 to C6 and then rotates back toward the film normal from C7 to C9 while also rotating within the plane of the film by several degrees. The R^{SL} vectors constitute a triclinic lattice. Therefore, the AL and SL vectors are necessarily non-collinear (as seen in Figure 3a; Table S2, Supporting Information). The R^{SL} shows a larger angular spread than the R^{AL} with orientation spread of 9.4° in-plane and 14.2° out-of-plane. This is an interesting result

because it shows that the AL orientations of the QDs are more uniform than would be expected from the SL position and orientation of the CoMs.

It is not known whether the epi-SL structure is determined thermodynamically, by minimization of the free energy, or whether the structure is kinetically trapped before complete relaxation. An energy minimized single crystal epi-SL structure would maximize the area overlap of the $\{100\}_{\text{AL}}$ facets between QDs and would eliminate atomic point defects and twist/tilt defects between NN QDs. Section S5 (Supporting Information) derives an expression for the minimized single crystal global structure ($R_{\text{mono}}^{\text{AL}}$) as a function of the SL positions and Table S3 (Supporting Information) shows how the unit cell changes with increasing mismatch between a cubic AL and triclinic SL. The $R_{\text{mono}}^{\text{AL}}$ for this epi-SL is depicted as a star in Figure 3a and the magnitude of the difference between $R_{\text{mono}}^{\text{AL}}$ and the measured R^{AL} is represented by the glyph color in Figure 2. The $R_{\text{mono}}^{\text{AL}}$ is almost identical to the average of the R_i^{AL} , which means that $R_{\text{mono}}^{\text{AL}}$ is a good representation of the average atomic orientation for the measured SL structure.

The systematic changes in R^{AL} from C1 to C9 suggest that there is no single lowest-energy AL/SL structure, but rather that different local R^{AL} are present due to differing forces in the surface and interior layers. Figure 3b shows an optimal alignment that maximizes the co-facial overlap with QD orientation nearly aligned to the substrate plane as seen in layers C1 and C9. Toward the interior layers, the average orientation misaligns into the non-optimal structure depicted in Figure 3b. To account for these changes in orientation, we also calculate a different energy minimized structure $\{\hat{R}_i^{\text{AL}}\}$ in which the CoMs are fixed at the measured P^{SL} and R^{SL} but the R^{AL} of each QD is oriented to maximize the overlap of the $\{100\}$ facets of the QDs. We then compare the mono-crystalline and multi-crystalline orientation optimizations to the measured R^{AL} using a Pearson correlation matrix and find a better correlation to $R_{\text{mono}}^{\text{AL}}$ than $\{\hat{R}_i^{\text{AL}}\}$. This means that the epi-SL is energetically driven toward $R_{\text{mono}}^{\text{AL}}$ and relatively insensitive to local SL randomness. The R^{AL} distribution is narrower than the R^{SL} distribution because the R^{AL} depends more on macroscopic forces than NN positions. This effect is demonstrated by the observation that QDs adjacent to a SL vacancy are not more randomly oriented than QDs with six nearest neighbors.

The AL orientation of each QD is driven toward an energetic minimum by reaching a balance between three factors: 1) maximizing the co-facial area of all $\{100\}_{\text{AL}}$ facets, 2) locally minimizing the nearest-neighbor AL misalignment, and 3) the surface layer orientations are fixed by the fluid/ligand interfaces during ligand exchange while interior layers reorient to an energy minimized structure. Thus, there are differing forces on surface and bulk QD layers that result in different structures. The next section examines the NN misorientation, which focuses on understanding the energetic driver for interior layer misalignment.

2.4. QD Orientation Analysis (Nanoscale)

A nanoscale approach to analyzing the AL/SL orientation begins by examining orientation at the NN level only. For

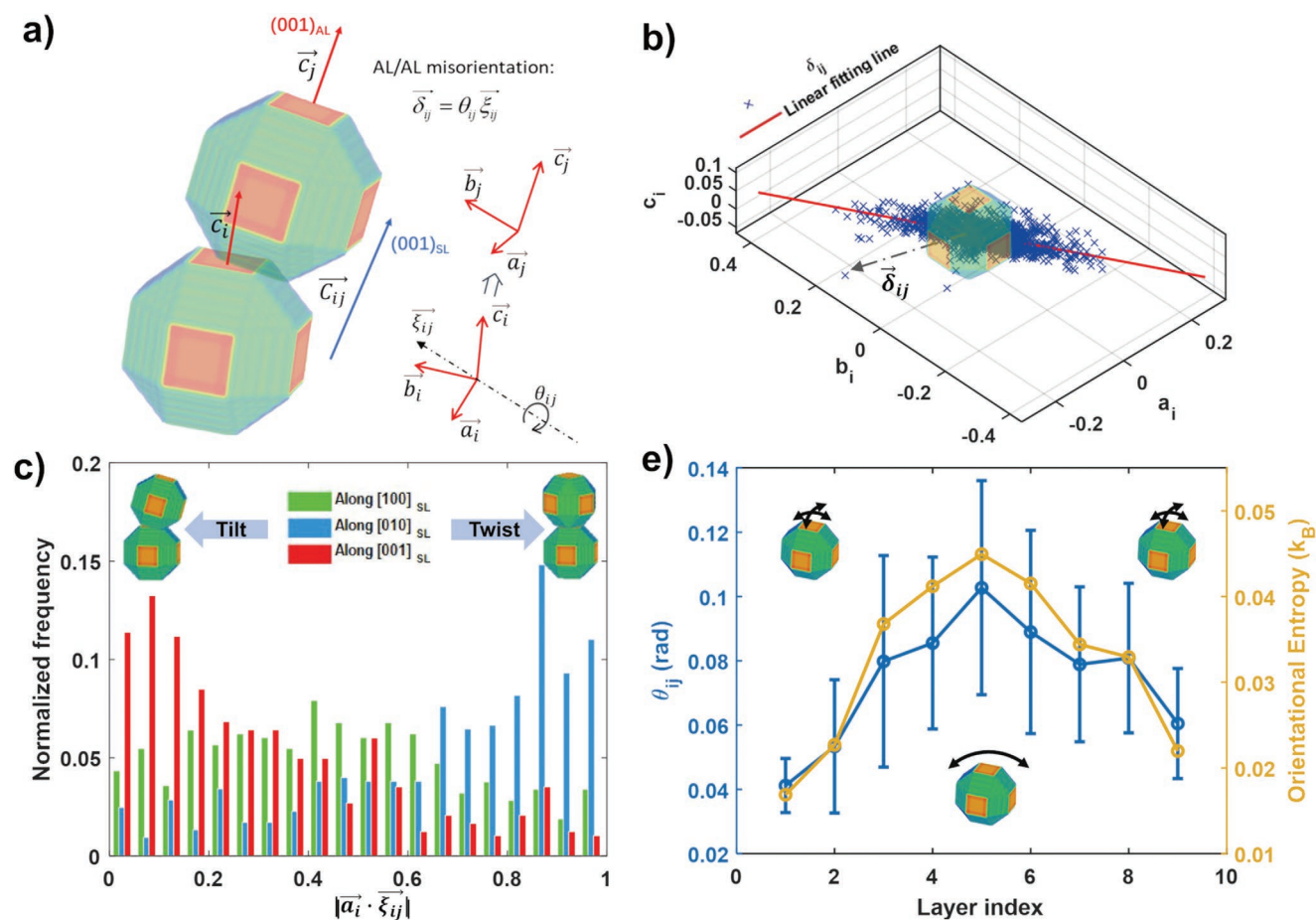


Figure 4. Nearest neighbor orientation disorder: a) Schematic showing the AL misorientation between nearest neighbor QDs. \vec{a}_i , \vec{b}_i , and \vec{c}_i denote $[100]_{AL}$, $[010]_{AL}$, and $[001]_{AL}$, respectively. b) Scatter plot and linear regression fit of $\vec{\delta}_{ij}$ (NN misorientation vector) expressed in terms of the components \vec{a}_i , \vec{b}_i , and \vec{c}_i . A QD is inset in the center of this panel for reference. c) Histograms of $|\vec{a}_i \cdot \vec{\xi}_{ij}|$ (cosine between the reorientation axis and the AL vector pertinent to the co-facet) showing distinct tilt/twist misorientation character along the different SL directions. Along $[100]_{AL}$ shows mixed tilt/twist, $[010]_{AL}$ shows primarily twist, and $[001]_{AL}$ shows primarily tilt misorientations. d) Depicts the NN misorientation magnitude θ_{ij} (blue) and orientational entropy (orange) as a function of the vertical layer index.

every pair of NN QDs, we define a NN misorientation vector $\vec{\delta}_{ij}$ as the product of a misorientation axis $\vec{\xi}_{ij}$ and a misorientation magnitude θ_{ij} (Figure 4a). In a perfect SL (as calculated in Section S5, Supporting Information), $\vec{\delta}_{ij}$ are all zero, whereas in a randomly oriented SL, an ensemble of $\vec{\delta}_{ij}$ occupies random points in a sphere. For the sample measured here, $\vec{\delta}_{ij}$ shows a distinct linear profile (Figure 4b), indicating the presence of a characteristic QD rotational axis $\langle \vec{\xi}_{ij} \rangle$ along $[\bar{1}20]_{AL}$. Principal component analysis (Section S7, Supporting Information) shows that this rotation axis explains 89% of the variance in the NN QD misorientations, meaning that the result is statistically significant and implies that nearly all of the QDs experienced the same systematic rotation. Abelson et al. previously reported that the QDs rotate around a common $[110]_{AL}$ axis during ligand exchange and epitaxial fusion.^[27] The difference in rotation axis ($[\bar{1}20]_{AL}$ versus $[110]_{AL}$) between this study and that of Abelson may be associated with the more distorted triclinic SL structure of this sample. More measurements are needed to verify this hypothesis.

A direct result of the characteristic reorientation axis is that the triclinic SL shows different ratios of tilt versus twist NN

misorientation components along different SL vectors. The dot product $|\vec{a}_i \cdot \vec{\xi}_{ij}|$ is a measure of the degree of tilt versus twist misorientation of each QD pair, with a value of zero indicating pure tilt and one indicating pure twist.^[23,46,47] Figure 4c shows a histogram of $|\vec{a}_i \cdot \vec{\xi}_{ij}|$ for every interface between the 633 QDs normalized for each of the three SL directions. In the out-of-plane direction ($[001]_{SL}$), there are more tilt misorientations (average dot product of 0.23), as would be expected from the analysis in Figure 3a. In-plane, Figure 4c shows a high degree of twist misorientation along $[010]_{SL}$ (average dot product of 0.78) but a nearly equal mixture of tilt/twist along $[100]_{SL}$ (average dot product of 0.44). The in-plane anisotropy of twist/tilt misorientation is further evidence that the QDs experienced a collective roll in the same direction during the ligand exchange process.

One remaining mystery from the tomographic data is to understand how layer index and orientation disorder are correlated. Figure 2d shows that C1 and C9 are most planar (have lowest position disorder) while C2 and C8 have the highest position disorder. In contrast, the R^{AL} changes gradually to the

center layers and does not show an abrupt change between the surface and interior layers. The layer dependent orientation disorder can be quantified by examining the misorientation magnitude (θ_{ij}) as a function of the layer index (Figure 4d), which shows considerably higher average orientation misalignment in the interior layers, consistent with the mesoscale analysis of QD orientation. But a higher average NN misorientation magnitude θ_{ij} is not the same as a broader distribution of alignments. A more direct measure of orientation distribution is orientation entropy, which quantifies the randomness of the orientation distribution in 3D space for each layer (Section S8, Supporting Information).^[48–50] Figure 4d shows that the orientational entropy and θ_{ij} follow the same trend. Both the average NN misalignment and the distribution of NN misalignments increase from C1 to C5 and decrease from C5 to C9. This last result shows that the position and orientation of the C1 and C9 interface layers remain more fixed during ligand exchange while the QDs in interior layers are more free to misorient. The volume reduction during ligand exchange results in a collective roll of the QDs along the $[1\bar{2}0]_{\text{AL}}$ direction that is more pronounced in interior layers. The contrast between surface

and interior layers also results in greater random misalignment (higher entropy) in the interior layers.

2.5. Kinetically Trapped Structure

In Table S3 (Supporting Information), we show images of the energy minimized epi-SL structures as a function of the triclinic angles. For every structure, the electronic disorder for the epi-SL is minimized by reduction of position disorder, SL orientation disorder, and AL orientation disorder. **Figure 5a** shows a schematic cartoon of the nine-layer stack showing the systematic change in AL orientation, a change that requires atomic lattice resolved tomographic measurement to capture. The fact that not all AL vectors are aligned and that center layers have different orientation shows that the epi-SL structure is kinetically trapped. There is an enthalpic driving force toward removal of high energy atomic dislocations between QDs, but the tilt and twist defects show that the epi-SL was frozen via NN neck formation before these defects could be resolved.^[23,47,51–54] The clear collective orientation behavior shows that the ligand

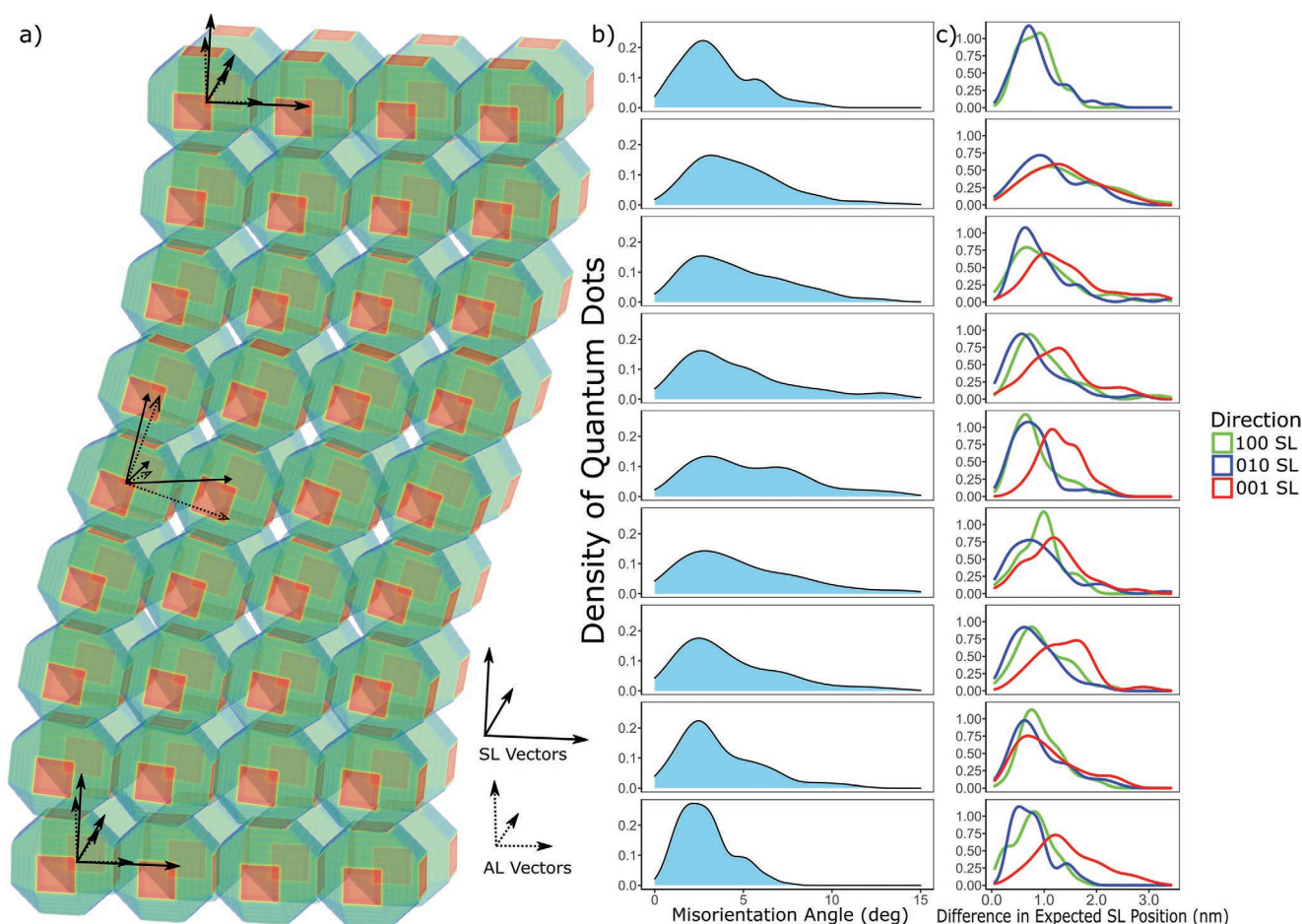


Figure 5. Kinetically trapped SL: a) Schematic showing the average AL and SL orientation for the multilayer film. A perfect triclinic SL (see Table S3, Supporting Information) has perfectly aligned AL interfaces. b) The distribution QD misorientation with respect to a fully aligned lattice as a function of layer index. c) The distribution of CoM positions (along $(100)_{\text{SL}}$, $(010)_{\text{SL}}$, and $(001)_{\text{SL}}$) with respect to a fully aligned lattice as a function of layer index. A perfectly positioned and aligned QD would have a value of zero in both distributions.

exchange is a collective topo-epitaxy^[41] and not by formation of NN attachments.^[55] Figure 5b,c shows the orientation and position differences, respectively, between the fully relaxed SL and the measured SL. Figure 5b shows that the QDs are on average misaligned by 2.5° but with a larger range of misalignment angles for center SL layers compared to surface layers. This is a second measurement of increased orientational entropy for center layers. Figure 5c shows the distance between the expected relaxed and actual QD location. Consistent with prior measurements, the top and bottom layers have a narrower distribution of differences compared to center layers. The largest position deviation even within each layer is along the [001]_{SL} direction, which is the same axis for the orientational anisotropy. Thus, all of the measurements point to a collective orientation change through the layers that are correlated with a specific rotation axis and increased position and orientation anisotropy in center layers.

3. Conclusion

We used large-volume, high-resolution electron tomography combined with Fourier analysis to generate the first lattice-resolved tomographic image of a 3D epitaxially-fused quantum dot superlattice. We resolved 633 QDs with 2.16 Å resolution, allowing for quantitative determination of QD position, orientation, and connectivity in three dimensions. Lattice-resolved tomography enables mapping of the orientations of the nanoscale building blocks of 3D mesomaterials, which was unfeasible until now. This new measurement capability will be enabling for emerging nanostructured energy storage, photovoltaic, gas storage, and catalyst materials.

A detailed analysis of the correlations between QD position, superlattice orientation, and atomic lattice orientation provides insight into the formation mechanism of the epi-SLs. We show that the surface layers have higher positional order, fewer superlattice point defects, higher nearest neighbor connectivity, and lower orientational anisotropy than the interior layers. The QDs in the surface layers are more oriented toward each other within the substrate plane and have more co-facial overlap between nearest neighbors. This result shows that measurements of epi-SLs that acquire surface information (e.g., 4D STEM) or average bulk information (e.g., GISAXS) can result in an incomplete and possibly misleading understanding of 3D nanostructured materials. Toward the interior layers, the average atomic lattice orientation rotates systematically out-of-plane, resulting in a tilted epi-SL that nonetheless maximizes the interfacial overlap, showing that the local atomic lattice orientational order is thermodynamically determined. Analysis of the nearest neighbor misalignment demonstrates a common in-plane rotation axis for QDs during the ligand exchange process. The average nearest neighbor misalignment, misalignment distribution, and orientational entropy all increase toward the center layers. These results have implications for fabrication of thicker and more perfect epi-SL samples. Ideally, the high position and alignment order of the surface layers would be found through the interior. The systematic "roll" of QDs in one direction and higher random misalignment, both of which are more pronounced in interior

layers suggests that the misalignment occurs as the superlattice is formed.

This work informs changes to the processing of epi-SL samples to reduce disorder and trigger mini-band formation. Here, we demonstrated that the mismatch between the cubic AL lattice and triclinic SL lattice reduces the nearest neighbor epitaxial overlap of the {100} facets. A logical method to improve epi-SL order should focus on controlling the ligand exchange kinetics to achieve a more cubic SL and reduce orientational entropy in interior layers.

Conflict Of Interest

The authors declare no conflict of interest.

Data Availability Statement

The data that support the findings of this study are available from the corresponding author upon reasonable request.

Supporting Information

Supporting Information is available from the Wiley Online Library or from the author.

Keywords

electron tomography, mesoscale, quantum dots, self-assemblies, superlattices

Received: February 2, 2023
Published online:

- [1] M. E. Davis, *Nature* **2002**, 417, 813.
- [2] A. S. Arico, P. Bruce, B. Scrosati, J. M. Tarascon, W. Van Schalkwijk, *Nat. Mater.* **2005**, 4, 366.
- [3] J. Lee, O. K. Farha, J. Roberts, K. A. Scheidt, S. T. Nguyen, J. T. Hupp, *Chem. Soc. Rev.* **2009**, 38, 1450.
- [4] A. Kudo, Y. Miseki, *Chem. Soc. Rev.* **2009**, 38, 253.
- [5] H. H. Tsai, W. Nie, J.-C. Blancon, C. C. Stoumpos, R. Asadpour, B. Harutyunyan, A. J. Neukirch, R. Verduzco, J. J. Crochet, S. Tretiak, L. Pedesseau, J. Even, M. A. Alam, G. Gupta, J. Lou, P. M. Ajayan, M. J. Bedzyk, M. G. Kanatzidis, A. D. Mohite, *Nature* **2016**, 536, 312.
- [6] A. Swarnkar, A. R. Marshall, E. M. Sanehira, B. D. Chernomordik, D. T. Moore, J. A. Christians, T. Chakrabarti, J. M. Luther, *Science* **2016**, 354, 92.
- [7] B. O'Regan, M. Grätzel, *Nature* **1991**, 353, 737.
- [8] C. K. Chan, H. Peng, G. Liu, K. McIlwrath, X. F. Zhang, R. A. Huggins, Y. Cui, *Nat. Nanotechnol.* **2008**, 3, 31.
- [9] G. P. Wang, L. Zhang, J. J. Zhang, *Chem. Soc. Rev.* **2012**, 41, 797.
- [10] K. S. Kumar, H. Van Swygenhoven, S. Suresh, *Acta Mater.* **2003**, 51, 5743.
- [11] Y. M. Wang, M. W. Chen, F. H. Zhou, E. Ma, *Nature* **2002**, 419, 912.
- [12] A. Devaraj, D. E. Perea, J. Liu, L. M. Gordon, T. J. Prosa, P. Parikh, D. R. Diercks, S. Meher, R. P. Kolli, Y. S. Meng, S. Thevuthasan, *Int. Mat. Rev.* **2018**, 63, 68.

- [13] L. Gross, F. Mohn, N. Moll, P. Liljeroth, G. Meyer, *Science* **2009**, 325, 1110.
- [14] D. N. Seidman, *Ann. Rev. Mater. Res.* **2007**, 37, 127.
- [15] F. Pfeiffer, *Nat. Photon.* **2018**, 12, 9.
- [16] A. Michelson, B. Minevich, H. Emamy, X. Huang, Y. S. Chu, H. Yan, O. Gang, *Science* **2022**, 376, 203.
- [17] H. Song, Y. Yang, J. Geng, Z. Gu, J. Zhou, C. Yu, *Adv. Mater.* **2019**, 31, 1801564.
- [18] R. S. R. Gajjala, P. M. Koenraad, *Nanomaterials* **2021**, 11, 1.
- [19] P. A. Midgley, R. E. Dunin-Borkowski, *Nat. Mater.* **2009**, 8, 271.
- [20] H. Han, S. Kallakuri, Y. Yao, C. B. Williamson, D. R. Nevers, B. H. Savitzky, R. S. Skye, M. Xu, O. Voznyy, J. Dshemuchadse, L. F. Kourkoutis, S. J. Weinstein, T. Hanrath, R. D. Robinson, *Nat. Mater.* **2022**, 21, 518.
- [21] J. Miao, P. Ercius, S. J. Billinge, *Science* **2016**, 353, aaf2157.
- [22] P. A. Midgley, M. Weyland, *Ultramicroscopy* **2003**, 96, 413.
- [23] M. A. Smeaton, I. El Baggari, D. M. Balazs, T. Hanrath, L. F. Kourkoutis, *ACS Nano* **2021**, 15, 719.
- [24] C. Ophus, *Micros. Microanal.* **2019**, 25, 563.
- [25] H. Yang, L. Jones, H. Ryll, M. Simson, H. Soltan, Y. Kondo, R. Sagawa, H. Banba, I. MacLaren, P. D. Nellist, *J. Phys.: Conf. Ser.* **2015**, 644, 012032.
- [26] K. Jarausch, P. Thomas, D. N. Leonard, R. Twisten, C. R. Booth, *Ultramicroscopy* **2009**, 109, 326.
- [27] A. Abelson, C. Qian, T. Salk, Z. Luan, K. Fu, J.-G. Zheng, J. L. Wardini, M. Law, *Nat. Mater.* **2020**, 19, 49.
- [28] W. J. Baumgardner, K. Whitham, T. Hanrath, *Nano Lett.* **2013**, 13, 3225.
- [29] C. W. Jiang, M. A. Green, *J. Appl. Phys.* **2006**, 99, 114902.
- [30] E. Kalesaki, W. H. Evers, G. Allan, D. Vanmaekelbergh, C. Delerue, *Phys. Rev. B* **2013**, 88, 115431.
- [31] C. S. S. Sandeep, J. M. Azpiroz, W. H. Evers, S. C. Boehme, I. Moreels, S. Kinge, L. D. A. Siebbeles, I. Infante, A. J. Houtepen, *ACS Nano* **2014**, 8, 11499.
- [32] K. Whitham, J. Yang, B. H. Savitzky, L. F. Kourkoutis, F. Wise, T. Hanrath, *Nat. Mater.* **2016**, 15, 557.
- [33] B. H. Savitzky, R. Hovden, K. Whitham, J. Yang, F. Wise, T. Hanrath, L. F. Kourkoutis, *Nano Lett.* **2016**, 16, 5714.
- [34] K. Whitham, T. Hanrath, *J. Phys. Chem. Lett.* **2017**, 8, 2623.
- [35] M. P. Boneschanscher, W. H. Evers, W. Qi, J. D. Meeldijk, M. Dijkstra, D. Vanmaekelbergh, *Nano Lett.* **2013**, 13, 1312.
- [36] H. Friedrich, C. J. Gommers, K. Overgaag, J. D. Meeldijk, W. H. Evers, B. D. Nijs, M. P. Boneschanscher, P. E. D. Jongh, A. J. Verkleij, K. P. D. Jong, A. V. Blaaderen, D. Vanmaekelbergh, *Nano Lett.* **2009**, 9, 2719.
- [37] B. H. Savitzky, K. Whitham, K. Bian, R. Hovden, T. Hanrath, L. F. Kourkoutis, *Micros. Microanal.* **2014**, 20, 542.
- [38] M. P. Boneschanscher, W. H. Evers, J. J. Geuchies, T. Altantzis, B. Goris, F. T. Rabouw, S. A. P. Van Rossum, H. S. J. V. Zant, L. D. A. Siebbeles, G. V. Tendeloo, I. Swart, J. Hilhorst, A. V. Petukhov, S. Bals, D. Vanmaekelbergh, *Science* **2014**, 344, 1377.
- [39] J. L. Peters, T. Altantzis, I. Lobato, M. A. Jazi, C. V. Overbeek, S. Bals, D. Vanmaekelbergh, S. B. Sinai, *Chem. Mater.* **2018**, 30, 4831.
- [40] X. Chu, H. Heidari, A. Abelson, D. Unruh, C. Hansen, C. Qian, G. Zimanyi, M. Lawand, A. J. Moulé, *J. Mater. Chem. A* **2020**, 8, 18254.
- [41] A. Abelson, C. Qian, T. Salk, Z. Luan, K. Fu, J.-G. Zheng, J. L. Wardini, M. Law, *Nat. Mater.* **2020**, 19, 49.
- [42] B. Goris, T. Roelandts, K. Batenburg, H. H. Mezerji, S. Bals, *Ultramicroscopy* **2013**, 127, 40.
- [43] R. Wirth, *Chem. Geol.* **2009**, 261, 217.
- [44] A. V. Baranov, E. V. Ushakova, V. V. Golubkov, A. P. Litvin, P. S. Parfenov, A. V. Fedorov, K. Berwick, *Langmuir* **2015**, 31, 506.
- [45] B. B. V. Salzmann, M. M. van der Sluijs, G. Soligno, D. Vanmaekelbergh, *Acc. Chem. Res.* **2021**, 54, 787.
- [46] W. Walravens, E. Solano, F. Geenen, J. Dendooven, O. Gorobtsov, A. Tadjine, N. Mahmoud, P. P. Ding, J. P. C. Ruff, A. Singer, G. Roelkens, C. Delerue, C. Detavernier, Z. Hens, *ACS Nano* **2019**, 13, 12774.
- [47] J. C. Ondry, M. R. Hauwiler, A. P. Alivisatos, *ACS Nano* **2018**, 12, 3178.
- [48] H. Felipe, A. Viol, D. B. de Araujo, M. G. E. da Luz, F. Palhano-Fontes, H. Onias, E. P. Raposo, G. M. Viswanathan, The von Neumann Entropy for the Pearson Correlation Matrix: A Test of the Entropic Brain Hypothesis. arXiv arXiv:2106.05379, **2021**.
- [49] J. Lee, J. Yang, S. G. Kwon, T. Hyeon, *Nat. Rev. Mater.* **2016**, 1, 16034.
- [50] E. Y. S. Chua, *Philos. Sci.* **2020**, 88, 145.
- [51] J. C. Ondry, L. B. Frechette, P. L. Geissler, A. P. Alivisatos, *Nano Lett.* **2022**, 22, 389.
- [52] J. C. Ondry, A. P. Alivisatos, *Acc. Chem. Res.* **2021**, 54, 1419.
- [53] Y. H. Lee, W. Shi, Y. Yang, Y.-C. Kao, H. K. Lee, R. Chu, Y. L. Pang, C. L. Lay, S. Li, X. Y. Ling, *Angew. Chem.-Int. Ed.* **2020**, 59, 21183.
- [54] J. J. Geuchies, G. Soligno, E. Geraff, C. P. Hendrikx, C. V. Overbeek, F. Montanarella, M. R. Slot, O. V. Kononov, A. V. Petukhov, D. Vanmaekelbergh, *Commun. Chem.* **2020**, 3, 28.
- [55] I. Y. Chen, J. C. daSilva, D. M. Balazs, M. A. Smeaton, L. F. Kourkoutis, T. Hanrath, P. Clancy, *ACS Nano* **2020**, 14, 11431.